Photovoltaic (PV) Solar Panel Identification and Fault Detection Using Unmanned Aerial

Vehicles (UAVs): A Case Study of a 0.5 MW PV System

Raymond Zhao

Advisor: Xuhui Lee

Second Reader: Michael Oristaglio

May 2, 2022

A Senior Thesis presented to the faculty of the Department of Earth and Planetary Sciences, Yale

University, in partial fulfillment of the Bachelor's Degree and requirements of the

Multidisciplinary Academic Program in Energy Studies at Yale College.

Photovoltaic (PV) Solar Panel Identification and Fault Detection Using Unmanned Aerial Vehicles (UAVs): A Case Study of a 0.5 MW PV System

ABSTRACT

Performance monitoring of individual PV modules in utility-scale solar farms can be a difficult undertaking due to the issue of scale. Since most PV systems are placed in-line and series connected, panel-specific granularity is costly and most systems monitor performance up to the inverter level. Because faulty PV modules are higher in temperature relative to the neighboring modules, unmanned aerial vehicles (UAVs) can play an important in this field because it can survey large areas within the RGB and infrared radiation (IR) wavelengths in a convenient and low-cost manner. In this study, we developed a workflow to capture UAV images, process the data, and perform panel identification and fault detection in the PV systems. We found that including a RGB dataset can greatly improve panel identification results since our algorithm utilizes ISODATA unsupervised classification. All of the 1048 panels were successfully identified, parsed, and turned into polygons. Moreover, our fault detection algorithm, using two spatial autocorrelation techniques, was able to detect 4 out of 6 faulty panels within our region of interest (ROI). Data validation was performed and we found that instantaneous mean temperature measurements did not have an intuitive relationship with energy output—positive relationship with an r-squared of 93%. It is very likely that the poor temporal resolution of the orthomosaic influenced instantaneous temperature measurements and temperature sensitivity to environmental factors like sunlight and cloud coverage. These results suggest that spatial information is quite important and should receive sizeable weight in fault detection techniques because temperature gradients within a ROI is robust. Furthermore, the use of Anselin Local Moran's I technique with the inverse distance squared method in our fault detection algorithm is valid because it utilizes spatial context to determine clusters and outliers.

TABLE OF CONTENTS

1. INTRODUCTION

1.1. Background

The positive long-run relationship between energy consumption and greenhouse gas emissions has been well studied and widely recognized (Azhar Khan et al., 2014; Hamit-Haggar, 2012). This trend is concerning because global energy demand is projected to increase dramatically in the next few decades as the world population grows and various countries become more developed (IEA, 2021). To decouple energy consumption and greenhouse gas emissions, policymakers have greatly focused on transforming the global energy mix—by reducing reliance on fossil fuels and harnessing renewable resources for energy generation (Mundaca et al., 2019). Currently, some of the most widely-utilized renewable resources around the world are solar, wind, geothermal, and hydropower (BP, 2021). The solar energy industry, in particular, has been growing at a dramatic rate (Hartmann et al., 2016). For instance, in the United States, solar is projected to make up 51% of all renewable electricity generation and become the most widely-utilized renewable resource by 2050 (Figure 1). The second most utilized renewable resource is projected to be wind, at 31% (U.S. EIA, 2022).

There are various forms of solar technology, but photovoltaics (PV) is the most popular. Individual PV modules typically have manufacturer warranty periods of up to 25-30 years but prolonged use and exposure to solar irradiation and temperature can cause reduced electrical power output and panel deterioration (Quater et al., 2014; Tsanakas et al., 2015). These defects come in various forms within the PV modules; visible failures can appear as delamination, bubbles, cracking, or yellowing while others like microcracks, snail trails, and shading can be hard to detect by visual inspection (Quater et al., 2014). When PV modules are in operation, defective cells within the panels typically have higher temperatures than normal cells around it (Kim et al., 2017;

Spagnolo et al., 2012; Vergura et al., 2015). Therefore, abnormal temperature gradients in infrared

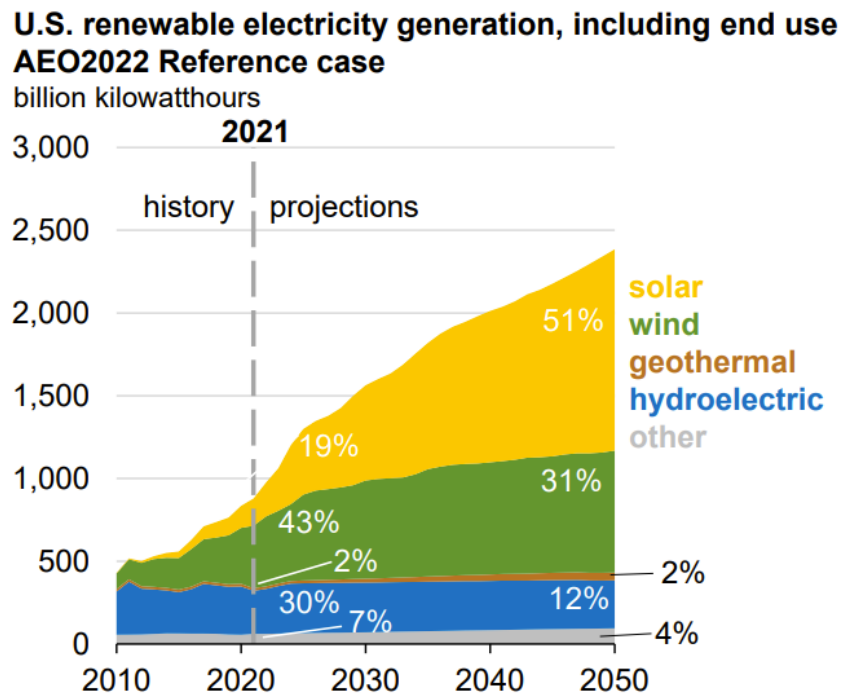(IR) images are a valid proxy for issues within PV module.

U.S. renewable electricity generation, including end use AEO2022 Reference case
billion kilowatthours

Figure 1. U.S. renewable electricity generation, including end use AEO2022 reference case. (Source: U.S. EIA, 2022).

Although visual inspection of PV arrays using IR thermography is a proven technique for

fault detection, it is not practical for large PV systems . Utility-scale PV plants with a rated capacity

of 1-20 MW typically require 34,000 m^2/MWac of land; while larger utility-scale PV plants, like

those with a rated capacity >20 MW, need 32,000 m^2/MWac of land (Ong et al., 2013). Another

technique for monitoring panel faults is using energy output measures; however, since most

utility-scale PV plants are often placed in-line and series connected, panel-specific detection is

hard due to data granularity issues (Kim et al., 2017). Unmanned aerial vehicles (UAVs) are able

to fill the niche for IR thermography application of panel-specific fault detection in utility-scale

PV plants. They are compact, convenient to use, and have a low operational cost. Moreover, the

images produced have higher spatiotemporal resolution compared to other remote sensing

platforms such as satellite and manned vehicles (Smith, 2015). Currently, UAVs are utilized in fields such as agriculture, archeology, forestry, hydrology, power infrastructure monitoring, and urban studies (Entrop & Vasenev, 2017; Herrmann et al., 2020; Kotivuori et al., 2020; Lu et al., 2022; Pecci, 2020; Santangeli et al., 2020; Tamminga et al., 2015; Tauro et al., 2016; Varghese et al., 2017; Vetrivel et al., 2015). UAVs have also recently become popular within the solar industry for various applications.

Prior to performing PV module fault detection, a panel detection method is required to select the regions of interest. There have been various PV panel detection algorithms developed. In Kim et al. (2016a), an automatic PV extraction algorithm used image segmentation techniques like horizontal, vertical, and morphological filtering. Other studies have utilized machine learning techniques like convolution neural networks (CNNs) to identify panels (Díaz et al., 2020). Since IR images are lower in resolution relative to RGB images, these algorithms are complicated to replicate. Moreover, they can vary in effectiveness depending on the resolution, which is affected by UAV flight parameters such as flight height and speed. Fault detection in panels has been approached through various avenues like statistical analysis of thermal intensity characteristics of each PV module and CNN-based models (Kim et al., 2017; Nie et al., 2020).

1.2. Objectives

In this study, my aim is to utilize UAV remote sensing and machine learning techniques to create a two-part algorithm that will first identify individual PV modules as polygons and then perform fault detection. In contrast to current literature, which use edge extraction methods (i.e.: Canny edge detector and Hough Transform) and machine learning techniques that require training sets (i.e.: CNNs) to delineate panel pixels from other pixels, our panel identification algorithm will utilize RGB and thermal data. Although RGB cameras are often built into UAVs and can provide

valuable spectral information, they are underutilized as most panel detection algorithms have only focused on using IR images to detect PV modules. Our fault detection algorithm will be performed using a combination of ArcGIS Pro, an industry standard for mapping-related operations, and Python within an ArcGIS-integrated Jupyter Notebook—which both have intuitive graphic user interfaces (GUIs) and will allow for easier reproducibility.

First, we operate an UAV to capture RGB and IR images of a 0.5 MW solar array. Second, we perform the 'Four-band Thermal Mosaicking' (FTM) technique, developed by Yang & Lee (2019), to create an image mosaic, also known as an orthomosaic, of the surveyed area. Third, Iterative Self-Organizing data Analysis Technique Algorithm (ISODATA) unsupervised classification is performed to label each pixel. Fourth, we develop an algorithm to identify individual PV panels. Fifth, an ArcGIS-based algorithm is created to detect possible faults in the PV panels. Lastly, we acknowledge our study limitations, validate our results, and discuss its industry implications.

1.3. Study Area

We surveyed a 0.5 MW ground mount PV system owned by Bishop's Orchards in Guilford, Connecticut, United States (Figure 2). Its coordinates are approximately 41.2896 N, 72.6966 W. The PV system went into operation on December 05, 2017. It has 8 inverters with a total of 1048 panels connected. The panel model is Trina Tallmax Plus TSM-325DD14A(II), and it has a rated power of 325W and an efficiency of 16.8%. The cell type is monocrystalline and the panel length, width, and depth are 1956 mm, 992 mm, and 40 mm, respectively. Every two panels are fitted with a 'SolarEdge Power Optimizer' which allows for performance monitoring at a two-panel granularity level. This is useful for energy output and fault validation purposes since PV system performance is generally monitored at the inverter level instead of the panel level (Orduz et al.,

2013). The study area imaged by the UAV has several surface types: bare soil, grass, PV modules, and snow.

(a)   (b)
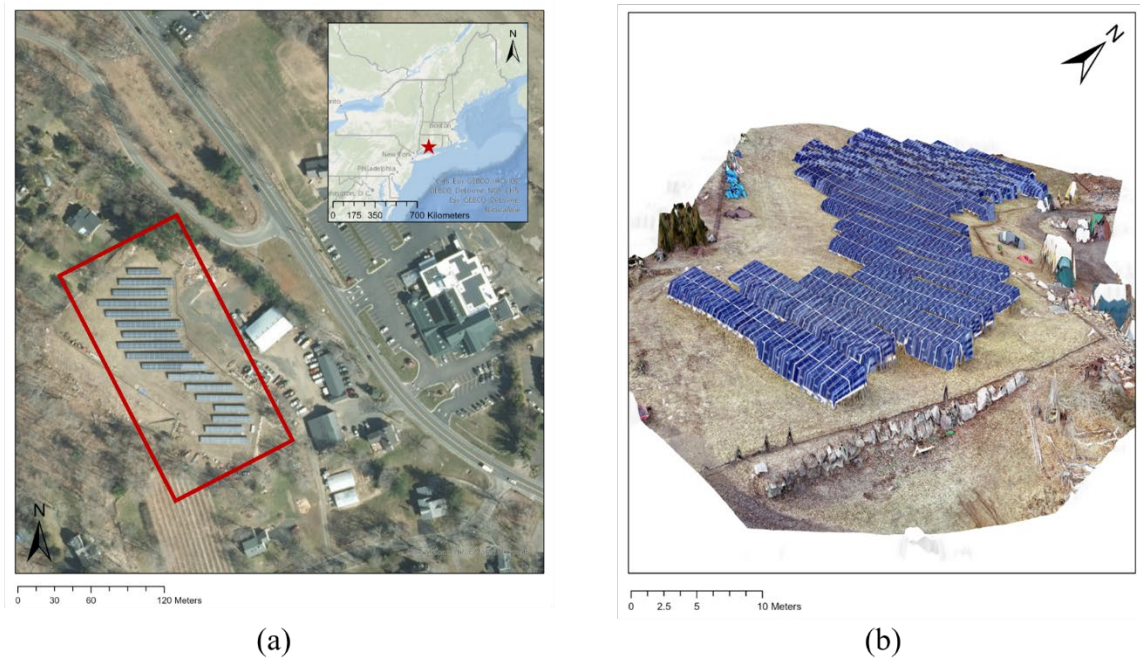
Figure 2. Study Area Maps. (a) This map is of Bishop's Orchard and the solar array. The red box depicts the approximate area surveyed by the UAV. The red start on the inset map depicts the approximate location of Guilford, CT. (b) The solar array is on a slight slope, as shown in the digital surface model (vertical exaggeration: 1.5x).

2. METHODS

2.1. Material & Instruments

A DJI Phantom 4 Pro Quadcopter was used to survey the PV system (Figure 3). Along with the built-in RGB camera, we also mounted on the FLIR DUO R dual-sensor RGB/IR camera. Both cameras took images in the nadir direction, and photos from both cameras were used. The DJI-RGB camera was synced with the DJI flight app and only images at optimized flight path locations were taken. The FLIR camera took images in its burst mode, which captures synchronized RGB and thermal image pairs every second. The RGB photos from the UAV (DJI-RGB) were saved in the 8-bit JPG format, the RGB photos from the FLIR camera (FLIR-RGB) were saved in the 8-bit JPG format, and the thermal images were saved in the 16-bit TIFF format. The resolution of the

DJI-RGB, FLIR-RGB, and thermal lenses are 5472x3648, 1920x1980, and 160x120 pixels. The DJI camera has a GPS sensor but the FLIR camera does not. Other materials included external batteries, propellers, UAV controller, and an iPad with the DJI flight app (Figure 3).
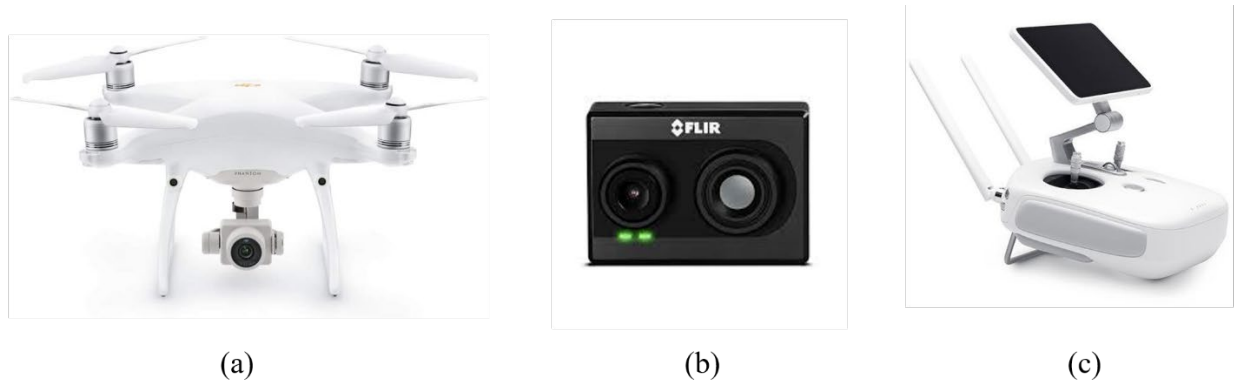

| (a) | (b) | (c) |

Figure 3. Materials and instruments. *(a) The DJI Phantom 4 Pro Quadcopter. It has an RGB camera. (b) FLIR DUO R. It has an RGB and IR camera. (b) The UAV remote controller with an iPad mini.*

2.2. Data

2.2.1. Flight

Our flight was conducted around 3:00 PM on March 10, 2022. The ambient temperature was around 7°C with 2.7 m/s winds coming from the northeast. The weather was partially cloudy with a relative humidity of 62%. These atmospheric conditions were inputted into the FLIR camera to correct for the effect of atmospheric absorption. Our flight route ran approximately parallel to the PV arrays, in the W-E direction. The UAV flew at 23 m above launch height with a flight speed of 5.4 m/s. The front and side overlaps were about 90% and 90% for both RGBs and thermal images. These parameters were chosen to optimize image quality over flight time efficiency; therefore, the whole flight took about 1.5 hours. Prior to image pre-processing, there were a total of 826 DJI-RGB images, 4,143 FLIR-RGB, and 4,143 thermal images (FLIR-IR).

2.2.2. Energy Output

Since every two panels were equipped with SolarEdge Power Optimizers, our energy production data was relatively granular. Our dataset was downloaded on March 9, 2022. It contains the daily energy output in Watt-hours, the current in amperes, and voltage in volts—along with the inverter number, panel model, and serial number. We took several steps to clean the data and summarize important statistics, specific to each inverter: count, aggregate energy output, and average kWh per panel.

2.2.3. Data Preprocessing
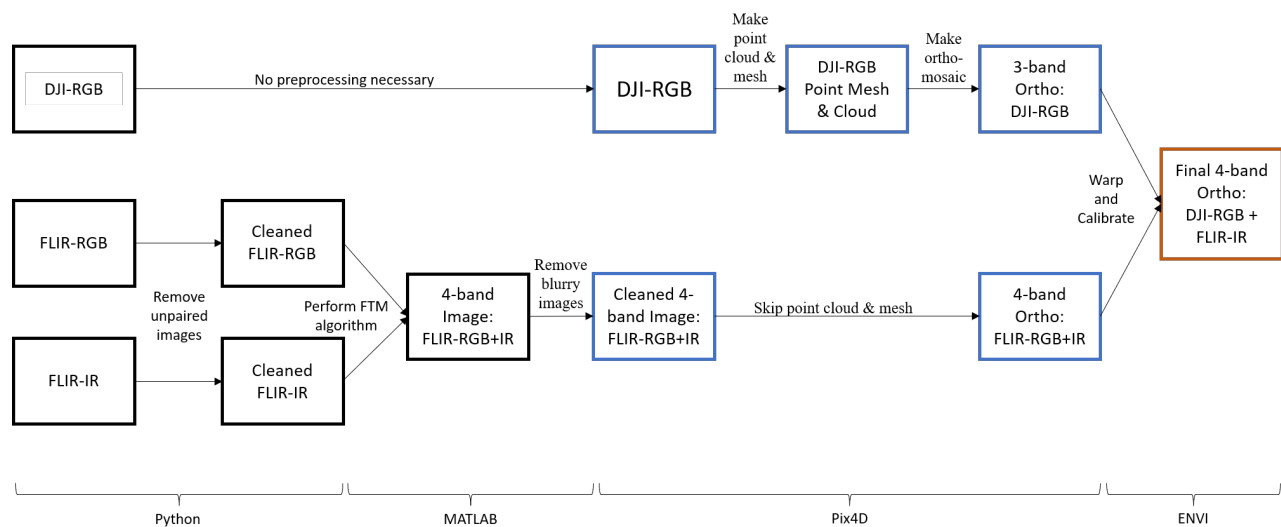
Figure 4. *This diagram depicts the workflow from preprocessing to orthomosaicking and then postprocessing—represented by the black, blue, and orange boxes, respectively.*

The DJI-RGB photos did not need to be preprocessed because they were already optimally taken by the UAV and geotagged. There were three preprocessing steps involved in cleaning the FLIR-RGB and thermal images (Figure 4). First, images that did not have RGB+IR pairs were removed; a filename matching algorithm in Python was created and performed since each pair has a unique name. A total of 14 FLIR-RGB images were removed because they didn't have corresponding thermal images. Second, the FTM algorithm was performed to combine the FLIR-

RGB and thermal images into one four-band image (Figure 5). Third, blurry images from ascent, descent, and turning of the UAV at the end of flight swaths were removed. The UAV was stationary at times throughout the flight, so images that were similar were manually removed to cut down on processing time. A total of 218 images were taken out.
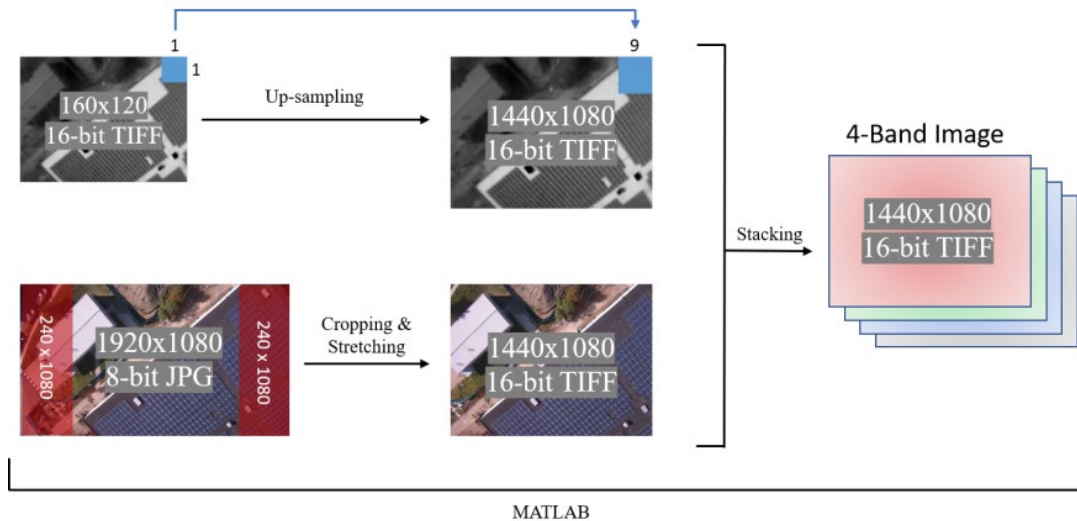

Figure 5. *This is the four-band thermal mosaicking algorithm. RGB and thermal images of a rooftop solar installation at one of Yale's West Campus buildings is used as the background for demonstrating the FTM process. It is important to note that the thermal image size is not proportional to the RGB image size. In reality, the thermal image is much smaller given its dimensions. This figure was adapted from figure 3 in Yang & Lee (2019).*

The FTM algorithm used was developed to overcome the difficult of mosaicking low-resolution, single-band thermal photos (Yang & Lee, 2019). Since the thermal and FLIR-RGB lenses have a vertical pixel resolution of 120 and 1080 pixels, respectively, it is valid to up-sample the thermal image by a factor of 9 to create a 9x9 matrix of pixels with identical Digital Number (DN) values. After up-sampling, the thermal image has a horizontal resolution (1440 pixels) that is slightly smaller than that (1920 pixels) of the FLIR-RGB image. Therefore, the FLIR-RGB image is cropped to the same size as the thermal image; it is then converted to the 16-bit 'TIFF' format with stretch multiplier of 10 to again match the thermal image format. Then the thermal band is combined with the visible band to create a four-band TIFF image with the sequence of red,

green, blue, and thermal IR. This FTM MATLAB algorithm developed in Yang & Lee (2019) was adapted and used to batch process all of the FLIR-RGB and thermal images.

2.2.4. Orthomosaicking and Postprocessing

The orthomosaicking workflow was performed in Pix4D, which uses a technique called 'structure-from-motion' (SfM) photogrammetry. This technique is a low-cost and innovative way to combine multiple images to form one large image called an orthomosaic (Iglhaut et al., 2019). In Pix4D, there are three steps to create an orthomosaic: Initial Processing, Point Cloud and Mesh, and then DSM, Orthomosaic, and Index.

In Initial Processing, the 3,925 four-band images were loaded in and several processing parameters were set to compute, calibrate, and match keypoints. The focal length was set to 34.8 mm since the FTM algorithm cropped the four-band image to the same Field of View (FOV) as the thermal image. Optimal band weights were inputted with the red, green, blue, and IR bands receiving 0.2126, 0.7152, 0.0722, and 0, respectively (Yang & Lee, 2019). The IR thermal band received no weight since it has a lower resolution and would reduce the accuracy of the mosaicking process. The Point Cloud and Mesh step creates a sparse point cloud which is then densified to control a 3D model of the measurement target (Yang & Lee, 2019). Although it is optimal to perform this step before orthomosaic generation, this step was skipped because it was RAM-intensive for the number of photos that we needed to process. The DSM, Orthomosaic, and Index step produced a digital surface model and orthomosaic with the 4-band images. In a similar fashion, the 826 DJI-RGB photos were processed into an orthomosaic using Pix4D. Because the DJI is a common UAV used for photogrammetry, the focal length, band weights, among other parameters were automatically set. The images went through all three steps because there were a relatively smaller number of images so we had sufficient RAM processing power. So, from the Pix4D

workflow, two orthomosaics were produced: DJI-RGB orthomosaic and the four-band orthomosaic (Figure 4).

Several postprocessing steps were performed. Because the DJI-RGB images had geotagging, it was a better orthomosaic than the RGB portion of the four-band orthomosaic. Moreover, since the FLIR-RGB has served its purposes in assisting the creation of a thermal orthomosaic, we decided to warp the thermal portion of the 4-band orthomosaic onto the DJI-RGB orthomosaic using the 'Warp and Resample' tool in ENVI (Figure 4). Through trial-and-error attempts, it was found that the optimal warping and resampling methods were 'resampling, scaling, and translation' (RST) and bilinear interpolation, respectively. Over 50 ground control points (GCPs) were chosen in each orthomosaic for the algorithm to use as tie points between the orthomosaics. Any GCPs with a root mean square (RMS) error greater than three was discarded. Because the original DJI-RGB photos were georeferenced, the DJI-RGB orthomosaic was georeferenced as well; subsequently, the thermal orthomosaic was automatically georeferenced while it was being warped with the DJI-RGB orthomosaic. Now, the DN values in the thermal layer need to be calibrated to temperature values in Celsius. In Yang & Lee (2019), a linear regression was performed between the DN value and sampled temperature measured using an infrared camera. The regression equation (equation 1) had an r^2 value of 0.82 and a p-value of 0.01. Given that the air temperature and sky conditions were similar between this flight and those in Yang & Lee (2019), it is valid to use equation 1 to perform the temperature calibration. This new orthomosaic, hereinafter referred to as the 'DJI-FLIR Orthomosaic', contains four bands with the RGB layers from the DJJI camera and the calibrated thermal layer from the FLIR camera. Moreover, it will be used for panel identification and fault detection.

$$\text{Sampled Temperature} = 0.024 * DN - 60.71 \tag{1}$$

2.3. Panel Identification and Fault Detection Algorithm

2.3.1. ISODATA Unsupervised Classification

The first step in our panel detection algorithm is to classify the pixels in the DJI-FLIR Orthomosaic. We used a popular remote sensing software called ENVI, which offers two machine learning unsupervised classification tools: K-Means and ISODATA. The K-Means method locates a user-defined amount of initial arbitrary cluster centroids and then assigns neighboring pixels according other minimum Euclidean distance. Moreover, the variability within clusters is minimized. The ISODATA method is similar to the K-Means method but without its disadvantages. Clusters are merged if their separate distance in multispectral space is below a certain threshold and the rule for splitting one cluster into two (El-Rahman, 2016; Sirat et al., 2019).

Given that ISODATA is a more refined type of unsupervised classification, it was chosen over the K-Means method to classify the RGB-FLIR Orthomosaic. There are several parameters to set for ISODATA classification: number of classes, maximum iterations, and change threshold. After several trails, it was found that 8 classes with a maximum of 10 iteration was optimal—from visual inspection, the panels did not share the same class with other surface types. The change threshold was kept at the default of 2%. Minor post-classification steps were taken to refine the classified image. The PV panels were contained in class 3 and class 4, and so they were grouped together. A mask was created to limit the region of interest to just the whole PV system. Lastly, the classes were renamed for visual convenience.

2.3.2. Panel Identification

Esri's ArcGIS Pro is the industry standard software for GIS-related tasks because of its intuitive user interface and wide array of tools. It also has an integrated Python environment (i.e.:

Jupyter Notebook) for automating workflows. Our panel identification workflow takes in an image with each pixel classified. All of the non-panel pixels are masked out using the 'Reclassify' tool.

Working with a raster that has pixels just in the PV panel class, we had to take out any noise such as misclassified pixels. To do this, every pixel must take on a region identity. The 'Region Group' tool was used for this zonal processing—connectivity was orthogonally defined, so every pixel that was connected on all four sides was grouped into a region. The 'Zonal Statistic' sum tool was iterated across every region group and the pixel counts for each region was generated. We converted the total pixel of each region to area in cm^2. Now that we have every pixel in a defined region, the noise can be addressed. We masked out all region smaller or larger than 1.5 standard deviations (SDs) from the median region size—assuming the median region size is the median size of a panel in the image. Because there are slight elevation changes relative to a constant flight height, the difference in panel size is expected.

This workflow isolates most of the PV modules; however, there are some issues in making the assumption that all PV panels will be 1.5 SDs from the median panel size. Regions that are 1.5 SDs below the median size are likely misclassified pixels; however, regions that are 1.5 SDs above the median size may be two panels combined. This can happen when misclassified pixels 'bridge' the two panels together by a strand of pixels. Therefore, a raster, of regions larger than 1.5 SDs from the median, was create and then focal statistics tools like "Shrink" and "Expand" were used to automate the refinement process to isolate out each PV panel region. After the panel refinement process, the regions were appended to the main raster with the rest of the isolated panels.

2.3.3. Fault Detection

Now that the previous workflow has produced a raster file with panels detected and noise removed, the fault detection workflow can proceed. Given the vastness of the study area, region

of interests (ROIs), defined as areas with panels that visually exhibit higher mean temperatures, are established. Within an ROI, the 'Zonal Statistics as Table' tool was used to calculate the re-calculate the mean temperature across each panel—this step is important for raster-to-polygon conversion purposes. Then, the output attribute table was joined with the raster with isolated panels. Finally, the raster file is converted to a polygon file.

For fault detection, we use two types of spatial autocorrelation techniques called Global Moran's I and Anselin Local Moran's I to look for specific panel temperature clusters and outliers. The former quantifies spatial autocorrelation of the whole defined region of interest while the latter measures spatial autocorrelation at specific locations within the region of interest. Both utilize Moran's I statistic, an indicator of spatial autocorrelation that ranges from -1 to 1. When Moran's I is a high positive number, the location of interest has similar values, either high or low, compared to its neighbors. Moreover, these are known as spatial clusters: high-high clusters or low-low clusters. When Moran's I is a high negative value, the location of interest has different values compared to its neighbors. They are known as spatial outliers: high-low or low-high outliers. If Moran's I statistic is zero, perfect spatial randomness is implied. The local Moran's I index can be expressed as (Anselin, 1995; Fu et al., 2014; Getis & Ord, 1992; Zhang et al., 2008):

$$I_i = \frac{z_i - \bar{z}}{\sigma^2} \sum_{j=1, j \neq i}^{n} [W_{ij}(z_j - \bar{z})] \tag{2}$$

The $\bar{z}$ represents the average of z with the sample value of n; z_i is the value of the variable at location I; z_j is the value of the variable where $j \neq i$; σ^2 gives the variance of z; W_{ij} is the distance weighting between z_i and z_j.

There are several parameters within ArcGIS Pro for using the Anselin local Moran's I tool. For the 'Conceptualization of Spatial Relationships' parameter, inverse distance squared was chosen because it gives more weight to nearby neighboring features than those farther away.

Moreover, taking the square of the inverse distance makes the influence of further features drop off more quickly (ArcGIS Pro, n.d.). Another important parameter for this tool is 'Permutations'. Random datasets are generated and compared to the Local Moran's I of the original data. A pseudo p-value is calculated because it looks at the proportion of the Local Moran's I statistics from permutations that have more clustering than that from the original data. Therefore, the more permutations, the more 'precise' the pseudo p-value will be (ArcGIS Pro, n.d.).

3. RESULTS

3.1. DJI-FLIR Orthomosaic

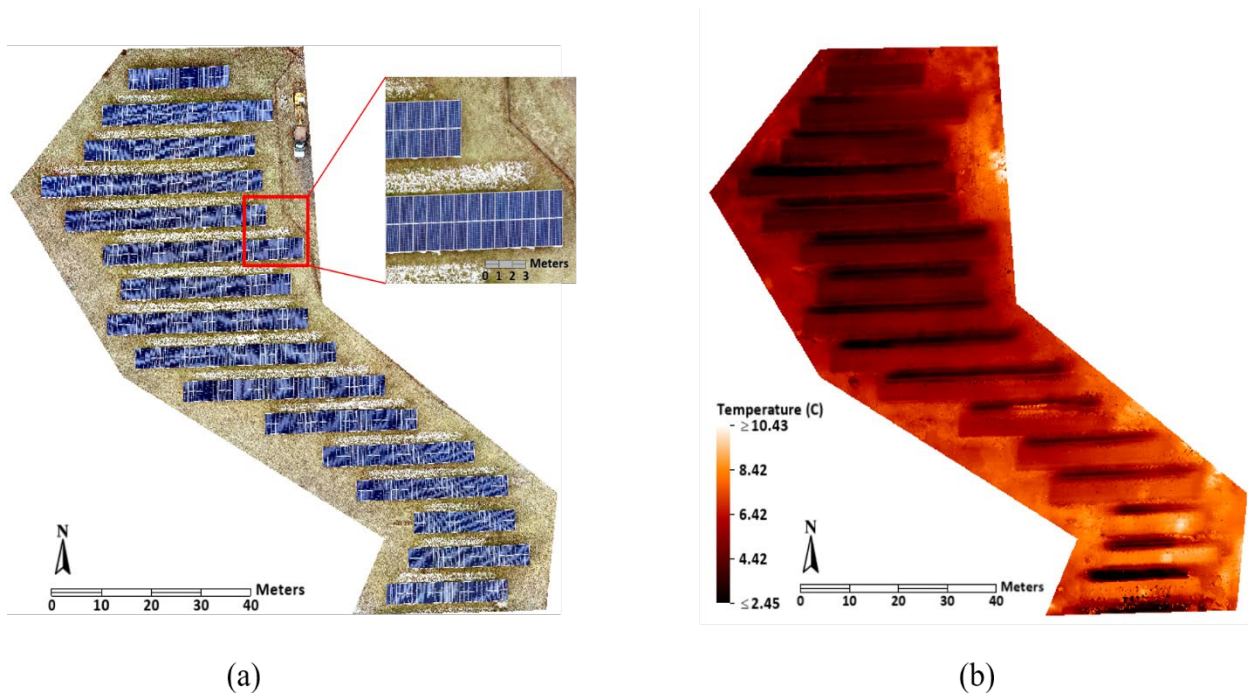(a)   (b)

Figure 6. DJI-FLIR Orthomosaic. *(a) This image contains the first three bands, DJI-RGB, of the 4-band orthomosaic. It looks pixelated but that is due to the linear patterns within the panels. A zoomed-in view of the panels is depicted by the red box. (b) The thermal band is the fourth band of the 4-band orthomosaic. Its DN values have been calibrated.*

The four-band orthomosaic has a pixel size of about 0.6 cm. Before cropping to the extent of the PV arrays, it contained a surveyed area that was around 9,900 m^2. There is a strong pattern between the RGB and thermal images (Figure 6). The PV modules are clearly depicted in the RGB

and corresponds with the distinct rows in the thermal image. Moreover, the panels are discernable in the thermal image because of the strong temperature contrasts between the PV modules and surrounding surface (Figure 6b.). The snow patches between the PV modules are associated with the lower temperature dark regions between the rectangular strips in the thermal images. Looking solely at the panels, there is a top to bottom temperature gradient that goes from colder panels to warmer panels, respectively. This slight gradient is also apparent in the surrounding surface, suggesting that the sun nontrivially affected the measured temperatures across the surveyed area.

Although the RGB orthomosaic appears pixelated, it is just that linear patterns of the PV cells create an illusion of pixels. A zoomed-in portion of the RGB orthomosaic was included to illustrated that the image itself is detailed and high definition (Figure 6a.). Another important aspect of the image to note is that the RGB and thermal image are stacked together in th four-band orthomosaic. Therefore, the subsequent analyses performed on the orthomosaic were done so considering all four data layers, unless otherwise noted.

3.2. ISODATA Classification and Panel Detection

ISODATA unsupervised classification successfully distinguished the PV modules from the surrounding surface within the four-band orthomosaic (Figure 7a.). The majority of the image is comprised of PV module pixels. The background is largely grass with patches of snow north of each panel. The location of the snow makes intuitive sense because the south facing panels likely blocked the sun from melting the snow, deposited from the snowfall during the night prior. Between each panel, there are pixels misclassified as snow. This is because the panels are bordered by a metal with low emissivity. Therefore, it has a lower apparent temperature reading and is categorized as snow. For the purposes of this study, this is negligible and does not need to be corrected for. Moreover, it is actually advantageous because all non-PV module pixels will be

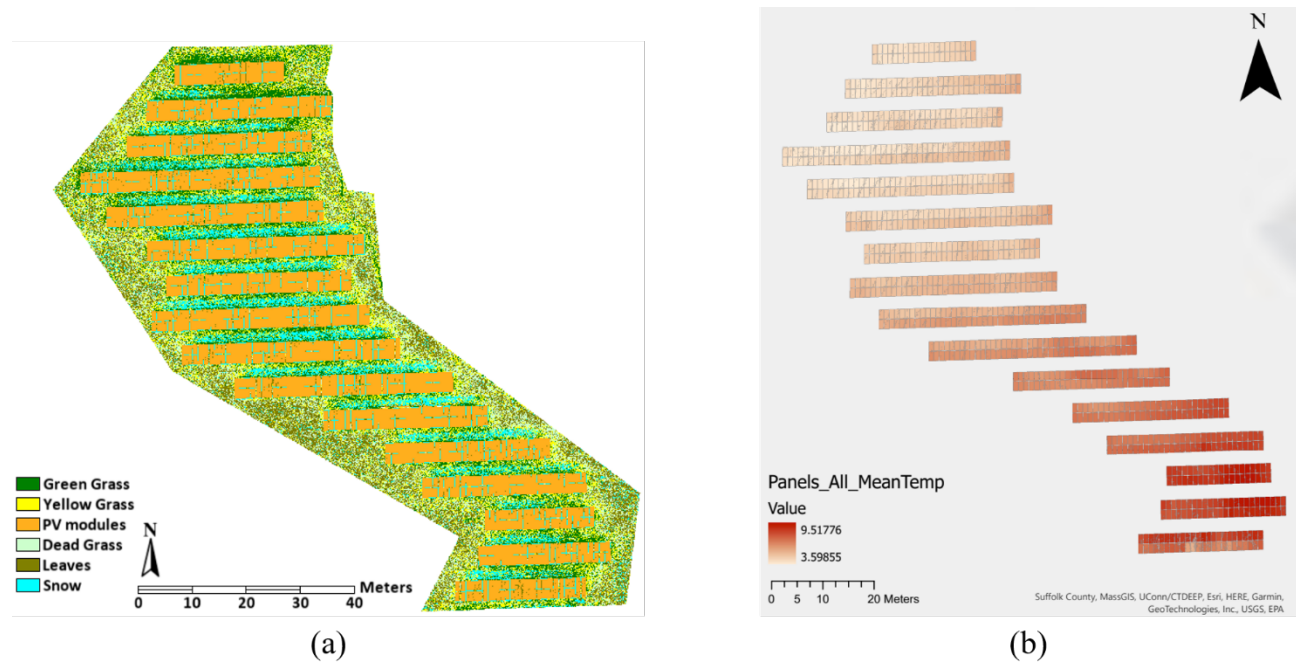masked out and the misclassified panel border pixels will serve to separate each panel for panel detection.

Figure 7. ISODATA Classification and the panel detection algorithm. *(a) There are 6 main classes within the classified image. The PV modules class is the one used in furthers steps. (b) After isolating pixels and removing noise, a raster with just panels was created. This map depicts the mean temperature for each of those panels.*

The panel detection workflow successfully singled out the 1048 panels in a raster file. This important step allows for iterative analysis across each specific PV panel. For example, in Figure 7b., mean temperature is measured and displayed across the panels. The raster can also be converted into polygon format for vector-based analysis techniques. The PV panels in Figure 7a. contain "holes" within the panels. It is negligible for mean temperature visualization and was not addressed; however, for fault detection, the holes were simply smoothed over to create uniform panel regions.

3.3. Fault Detection

The lower right corner of the PV system was chosen as the region of interest for further analysis, since visual inspection shows that there are higher mean panel temperatures there (Figure

7b.). The results of the Global Moran's I analysis revealed that there were statistically significant clusters within the region of interest—given a p-value of 0 and an alpha value of 0.01, the null hypothesis that the mean PV panel temperatures are randomly spatially-distributed is rejected (Figure 8). Moreover, the Moran's I index is approximately 1, which means that there are clusters of similar temperature data within the region of interest. Therefore, we proceeded with the Anselin Local Moran's I analysis to determine which specific panels are statistically significantly clustered.

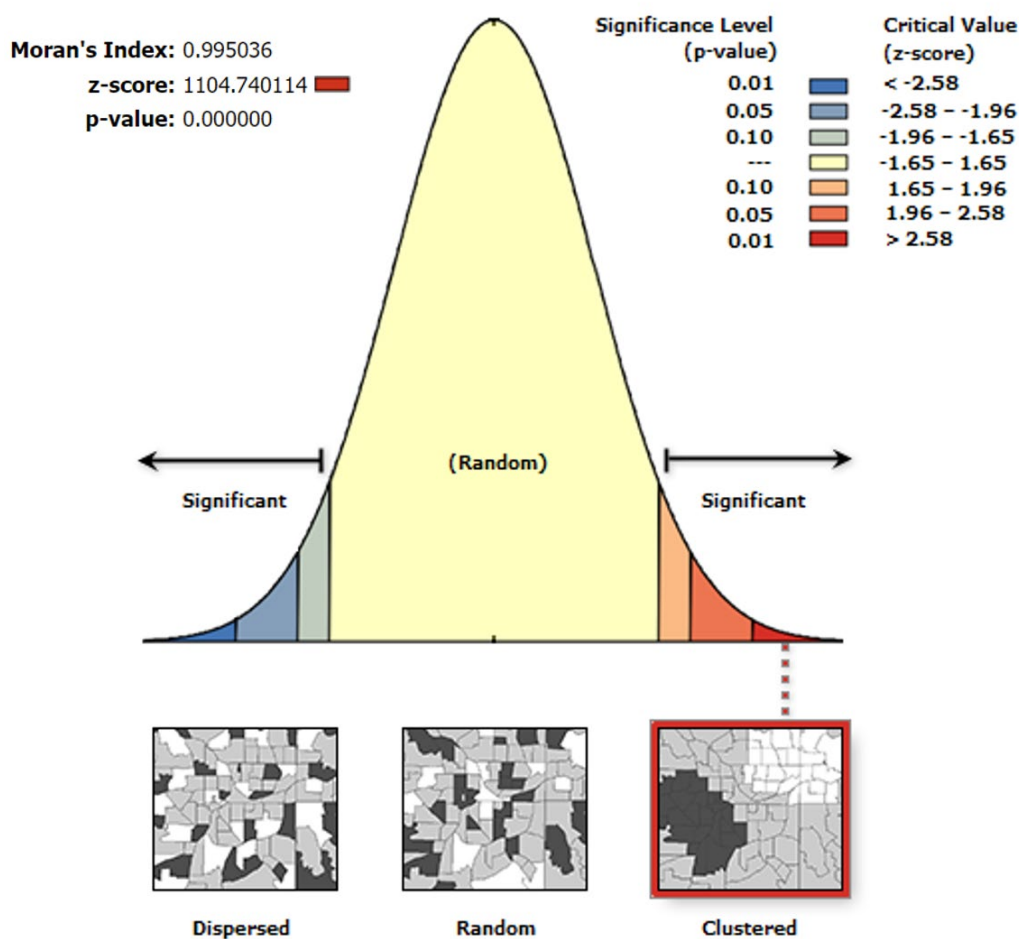**Figure 8.** *Results of Global Moran's I analysis. The red box around 'clustered' indicates that our ROI has clustered patterns for mean temperature. Since the p-value is practically 0, the null hypothesis is rejected.*

Anselin Local Moran's I with inverse distance squared spatial relationships and zero permutation produced the best results. Faulty panels were defined as those with little to no energy

output during the flight. Because the instantaneous energy data that we obtained was granular up to every two panels, this fault detection analysis was able to validated. There was a total of 6 faulty panels within the region of interest (Figure 9). In Figure 9a., the inverse distance squared method with zero permutation was used. It was able to detect 4 true positives, and it also categorized 2 false positives. It was not able to detect 2 true positives—panels 5 and 6 in Figure 9a. In Figure 9b., the k nearest neighbors method with zero permutations was used. The default of 8 neighbors was kept. It produced 4 true negatives and 6 false positives. It also did not detect 2 true positives— panels 5 and 6 in Figure 9b—and a high-low outlier. In general, zero permutation were used because increasing the number of permutations also increased the 'sensitivity' of the tool and more false positives were present.

(a)   (b)
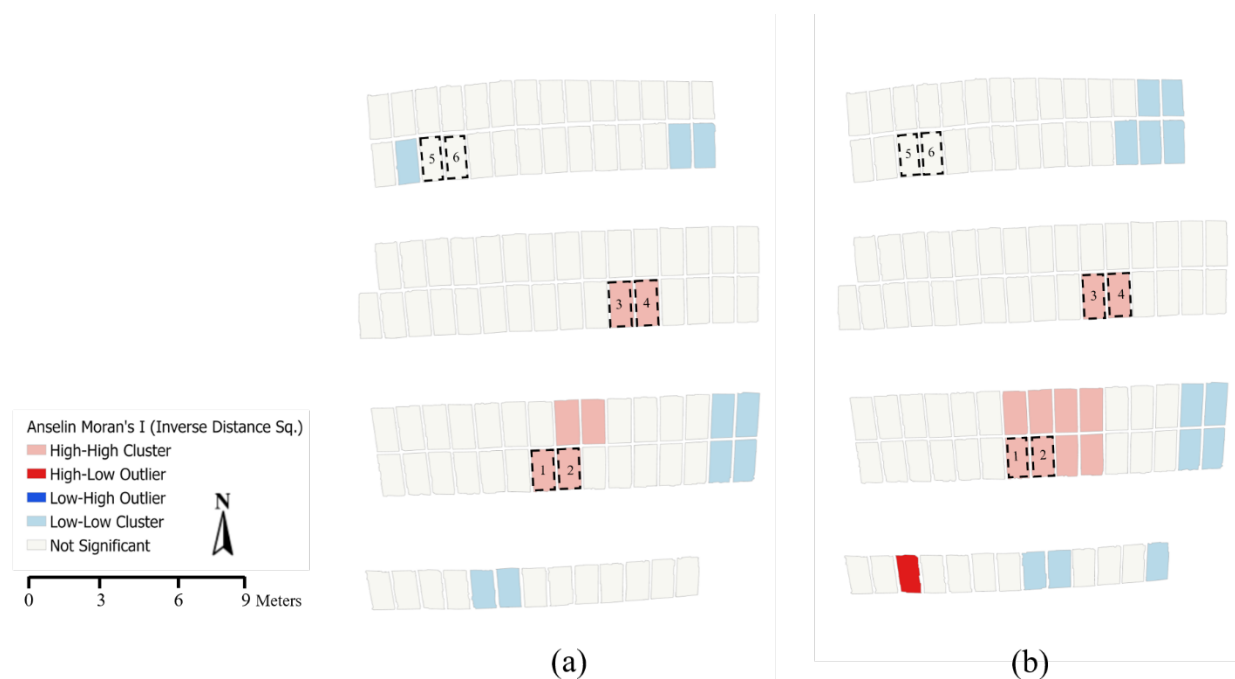
Figure 9. Fault detection results. *(a) The inverse distance squared method was used, along with 0 permutations. 6 total high-high clusters were identified, two of which were false positives. Two false negatives were identified. (b) The k nearest neighbors method was used, along with 0 permutations. Many more high-high clusters were found. Also, a high-low outlier was identified. In general, the low-low clusters were assumed to be the same as "not significant'.*

3.4. Data Validation

3.4.1. Validating Panel Identification and Fault Detection

There were 1048 total panels within the final raster created from the panel identification workflow. This matches the number of panels that were present within the image. Therefore, the algorithm used for singling out each individual panel was valid.

Table 1

Confusion Matrix (Fault Detection)

		Predicted		
		Faulty	Not Faulty	Actual Total
	Faulty	TP: 4	FN: 2	6
Actual	Not Faulty	FP: 2	TN: 94	96
	Predicted Total	6	96	-

Note: TP = true positive, FP = false positive, FN = false negative, TN = true negative.

A confusion matrix, traditionally used for quantifying classification results, was produced to quantify the fault detection process (Table 1). The total number of predicted faulty panels and actual faulty panels are equal. However, this is because two were misrepresented as faulty panels and two other true faulty panels were not detected (Figure 9a. and 9b.). Moreover, these results produced several values: sensitivity (0.667), specificity (0.979), precision (0.667), accuracy (0.961), F1 score (0.667), and Matthews Correlation Coefficient (0.646).

3.4.3. Temperature and Energy Production

One major assumption in this study was that there is a relationship between PV module temperature and its productivity—an inverse relationship is expected since a higher temperature relative to its neighbors means that a panel is likely faulty. Therefore, it is important to look to see

if the relationship between temperature and energy production is intuitive. The temperature distribution across all the panels is right-skewed (Figure 10a). The temperature distribution for the region of interest is relatively normal distributed with a slight left-skewed, given that the median is to the right of the mean (Figure 10b.). Moreover, notice that there are a few panels with higher temperatures that seem to be clustered to the right of the histogram.

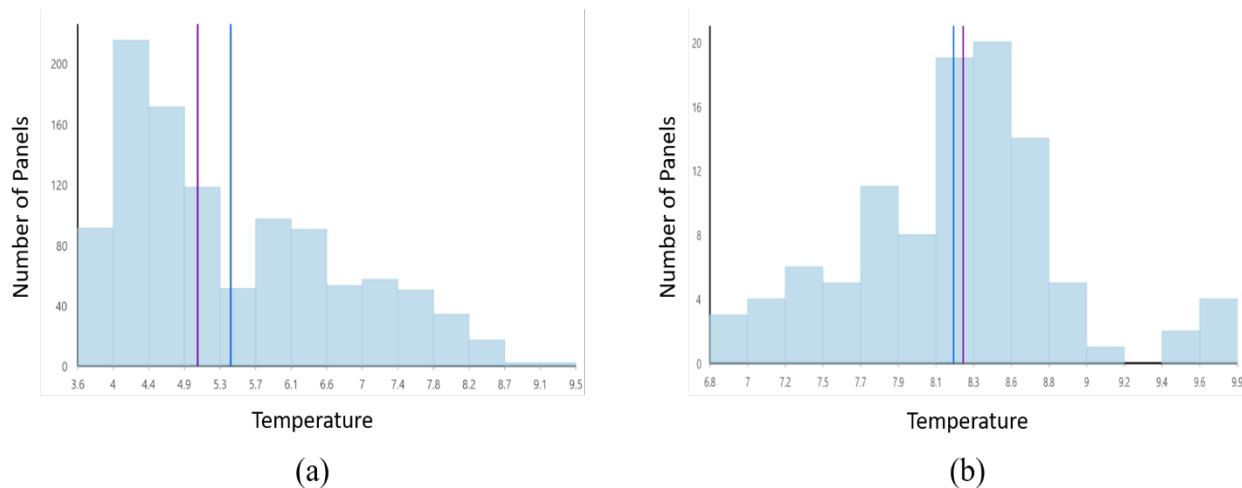(a)   (b)

Figure 10. Temperature histograms. (a) This histogram depicts the temperature distribution across all the panel at Bishop's Orchard. There is a right-skew to the data. (b) This histogram depicts the temperature distribution across the ROI in the southern right corner of the PV system. It normally distributed but there is a slight left skew.

A simple linear regression was performed between daily energy output per panel and mean temperature (Figure 11). These variables are grouped by inverter. Although there are only 7 data points, this is sufficient because the values were calculated by averaging all of the panels within the inverters—with each inverter having around 69 panels. It was grouped this way because joining mean temperature with energy output was difficult at the panel-panel granularity level. In the linear regression, the r-squared value is around 93% (Figure 11). Moreover, 93% of the variability in energy output is explained by the mean temperature. Since the p-value is smaller than an alpha value of 0.01, the positive relationship between energy output and mean temperature is statistically significant. Although there is strong evidence for this positive relationship, it is not intuitive.
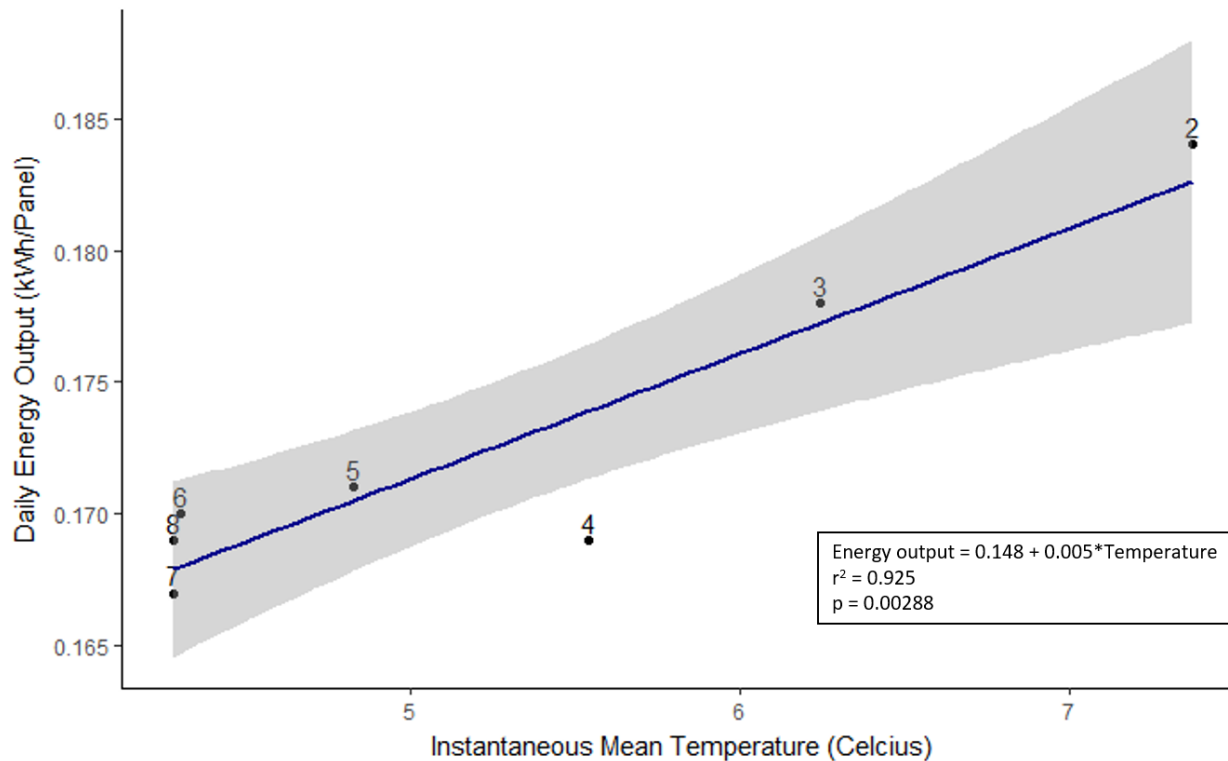
Figure 11. *Linear regression plot of mean temperature and energy output per inverter. The gray band is the 95% confidence band. Each number corresponds with an inverter number. The regression equation, r^2, and p-value are given in the box.*

4. DISCUSSION

4.1. Energy and Temperature

It has been established through empirical observations and academic studies that when a PV module is faulty, it will be higher in temperature relative to the other panels around it (Kim et al., 2017; Spagnolo et al., 2012; Vergura et al., 2015). However, this was not observed in the linear regression performed between mean temperature and energy output of the panels (Figure 11). There are several reasons that this may be the case. It is possible that grouping temperature and energy output by inverter, instead of by panel, created a false trend given the broader scope of the analysis. It may also be that temperatures are only significantly higher when there are faulty panel—and since most panels were functioning normally, it was not evident in the mean temperature values across inverters. However, the most influential reason why the linear regression

results are not intuitive is likely because the temporal resolution of the variables is quite different. Given that the mean temperature values are near-instantaneous snapshots of the panel temperatures, it has poor temporal resolution compared to the daily energy output values. Therefore, it is much more sensitive to factors like sunlight affecting its values. The UAV flight lasted over an hour and that affected temperature readings more than faulty panels would have. These observations reveal that instantaneous temperature readings may not be a great proxy for energy output. Rather, mean temperature within a PV panel over a longer time period may produce more intuitive results.

Within the context of fault detection, temporal resolution is not a limiting factor. This is evident through the fact that the fault detection algorithm in ArcGIS Pro was able to identify clusters of hot panels which correlated with the true faulty panels (Figure 10). In fact, the linear regression results strengthen the case for including spatial information into fault detection. The Anselin Local Moran's I technique, with the inverse distance squared method, finds clusters but gives more weight to panels that are closer to the clusters of interest. Therefore, spatial information (i.e.: temperature gradients between panels) is more important than just looking at mean temperature values with no spatial context.

4.2. Limitations

There were several constraints within our study that are important to note. Our flight took around an hour and a half, which is quite long for a relatively small study area. Due to limited time, we decided to optimize image quality over flight efficiency to prevent the possibility of going back to perform more flights. Optimization of image overlap with flight time is a process that involves making assumptions because cameras can have different FOVs and are offset from each other. In our case, we used a 90% by 90% overlap which increase flight time. There is literature that focuses

on these issues that should be implemented in future work (Grimaccia et al., 2015; Leva et al., 2015; Luo et al., 2017).

During the orthomosaic process, we discovered that hardware is an important factor in processing large datasets. We had to skip the 'point cloud and mesh' step for generating the FLIR RGB+IR four-band orthomosaic because it was RAM-intensive—we had 64 GB of RAM and it was not enough. This reduced the quality of the final orthomosaic; the southernmost row of PV panels was removed during postprocessing since they were close to the edge of the orthomosaic, where distortions occurred and DN values were not reliable. This problem can be addressed through flight optimization, which will reduce the number of images in the flight dataset. Moreover, other photogrammetry software like Agisoft Metashape and RealityCapture can be used if they require less RAM for image processing.

Another limitation within our study was that we had an optimal dataset to work with, in terms of PV module coverage, because there were no objects in the way between the camera and PV modules. In other studies, algorithms accounted for obstructions like powerlines, shade, and sun glint (Díaz et al., 2020). In future studies, our unsupervised classification method should be performed on RGB+IR orthomosaics that contain objects that occlude PV modules from the camera view, so that additional steps are added to the panel detection algorithm to address these issues. Moreover, these new study sites will ideally have more faulty panels for data validation purposes.

4.3. Industry Implications

We introduced several novel applications of techniques for data processing, panel identification, and fault detection throughout our study. Most studies have only utilized the thermal image to conduct panel identification and fault detection (Díaz et al., 2020; Kim et al., 2016a,

2016b). Because of its lower resolution, more complicated techniques need to be implemented to distinguish and, furthermore, create panel polygons. Using machine learning (i.e.: unsupervised classification) and an additional RGB data layer, panel detection can be a lot simpler—unsupervised classification does not need training sets nor need to establish panel borders through line detection techniques.

ArcGIS Pro was the main software that we used for fault detection analysis since it is heavily integrated in the spatial and GIS-related fields. Therefore, it will be easily accessible to those within this industry. Moreover, because this process can be automated within the ArcGIS-integrated Jupyter Notebook, fault detection can be conveniently performed. In fault detection algorithm, Anselin Local Moran's I was used. Although this technique has been applied to large-scale spatial analyses, we proposed a different application of this technique by implementing it for small-scale cluster and outlier analyses (Chen et al., 2020; Fu et al., 2014; Shariati et al., 2020; Zhang et al., 2008). Because this technique is able to identify faulty panel clusters, as shown in Figure 10, it may prove useful for industry-based implementation.

5. CONCLUSION

UAVs will play an important role in the utility-scale PV solar farm industry. As PV systems get larger, performance and fault monitoring will become more difficult but the convenience and affordability of the UAV fills a niche in the field. In our study, we conducted a UAV flight for data collection, and then we developed our own panel identification and fault detection algorithm. Most of the algorithm was performed in Python and ArcGIS. We found that adding an RGB layer greatly improves panel detection, compared to thermal-only scenarios. Moreover, ISODATA classification is a simple but effective machine learning algorithm to distinguish PV module pixels.

Global Moran's I and Anselin Local Moran's I are powerful cluster and outlier analysis techniques, especially when they are used in conjunction with each other. Moreover, they are applicable to small-scale operations like detection of faulty panels. Within our ROI, Anselin Local Moran's I was able to identify 4 of the 6 faulty panels. Moreover, 2 non-faulty panel were miscategorized. In the context of a confusion matrix, the fault detection algorithm has a sensitivity of 0.667, accuracy of 0.961, and a Matthews Correlation Coefficient of 0.646.

We discovered that instantaneous mean panel temperature may not be a great indicator of energy production because the positive linear relationship between the two variables is not intuitive. Other factors such as time of day and cloud coverage can greatly affect the instantaneous temperature of the panel. For proper comparisons, the two variables should have similar temporal resolutions. These results, however, strengthened the fact that spatial information (i.e.: temperature gradients) is important within fault detection. Spatial gradients are robust and aren't prone to issues caused by poor temporal resolution—especially if the Anselin Local Moran's I technique is used within a ROI.

It is evident that there are various applications for our panel identification and fault detection techniques within the field. Future work should involve testing out the algorithm on other PV system datasets. Moreover, the range of software used can be condenses for consistency and ease of access. For instance, much of the data postprocessing that was performed in ENVI can be adapt to the ArcGIS Pro environment. In literature, there's been more research done on real-time monitoring instruments and techniques, especially for series-connected PV systems (Moreno-Garcia et al., 2016; Ochiai & Ikegami, 2016). UAV-based fault detection techniques, coupled with different types of granular on-site monitoring systems, will be an efficient method for utility-scale PV system performance monitoring.

ACKNOWLEDGEMENTS

I would like to thank Professor Xuhui Lee, my advisor and first reader, for his expertise and guidance throughout the past two semesters. I would also like to acknowledge Professor Michael Oristaglio, my second reader, for his leadership in the Energy Studies program and for the role he played in sparking my interest within the renewable energy sector. The completion of my thesis would not have been possible without the kind support of so many people whom I have the deepest appreciation for: Professor Maureen Long, Professor Pincelli Hull, Tarek Kandakji, Yichen Yang, Eric Chien, other EPS faculty, Yale Out of the Blue A Cappella groupmates, friends, and family. Lastly, I'd like to thank the EPS department for funding our work through the Karen L. Von Damm '77 Undergraduate Research Fellowship in Earth and Planetary Sciences.

REFERENCES

Anselin, L. (1995). Local Indicators of Spatial Association—LISA. *Geographical Analysis*, *27*(2), 93–115. https://doi.org/10.1111/J.1538-4632.1995.TB00338.X

ArcGIS Pro. (n.d.). *Cluster and Outlier Analysis (Anselin Local Moran's I) (Spatial Statistics) Documentation*.

Azhar Khan, M., Zahir Khan, M., Zaman, K., & Naz, L. (2014). Global estimates of energy consumption and greenhouse gas emissions. *Renewable and Sustainable Energy Reviews*, *29*, 336–344. https://doi.org/10.1016/J.RSER.2013.08.091

BP. (2021). Full report – Statistical Review of World Energy 2021. *BP Statistical Review of World Energy*. https://www.bp.com/content/dam/bp/business-sites/en/global/corporate/pdfs/energy-economics/statistical-review/bp-stats-review-2021-full-report.pdf

Chen, Z., Jiang, Y., & Sun, D. (2020). Discrimination and Prediction of Traffic Congestion States of Urban Road Network Based on Spatio-Temporal Correlation. *IEEE Access*, *8*, 3330–3342. https://doi.org/10.1109/ACCESS.2019.2959125

Díaz, J. J. V., Vlaminck, M., Lefkaditis, D., Vargas, S. A. O., & Luong, H. (2020). Solar panel detection within complex backgrounds using thermal images acquired by uavs. *Sensors (Switzerland)*, *20*(21), 1–16. https://doi.org/10.3390/s20216219

El-Rahman, S. A. (2016). Hyperspectral imaging classification using ISODATA algorithm: Big data challenge. *Proceedings - 2015 5th International Conference on e-Learning, ECONF 2015*, 247–250. https://doi.org/10.1109/ECONF.2015.39

Entrop, A. G., & Vasenev, A. (2017). Infrared drones in the construction industry: designing a protocol for building thermography procedures. *Energy Procedia*, *132*, 63–68.

https://doi.org/10.1016/J.EGYPRO.2017.09.636

Fu, W. J., Jiang, P. K., Zhou, G. M., & Zhao, K. L. (2014). Using Moran's i and GIS to study the spatial pattern of forest litter carbon density in a subtropical region of southeastern China. *Biogeosciences*, *11*(8), 2401–2409. https://doi.org/10.5194/BG-11-2401-2014

Getis, A., & Ord, J. K. (1992). The Analysis of Spatial Association by Use of Distance Statistics. *Geographical Analysis*, *24*(3), 189–206. https://doi.org/10.1111/J.1538-4632.1992.TB00261.X

Grimaccia, F., Aghaei, M., Mussetta, M., Leva, S., & Quater, P. B. (2015). Planning for PV plant performance monitoring by means of unmanned aerial systems (UAS). *International Journal of Energy and Environmental Engineering*, *6*(1), 47–54. https://doi.org/10.1007/s40095-014-0149-6

Hamit-Haggar, M. (2012). Greenhouse gas emissions, energy consumption and economic growth: A panel cointegration analysis from Canadian industrial sector perspective. *Energy Economics*, *34*(1), 358–364. https://doi.org/10.1016/J.ENECO.2011.06.005

Hartmann, H. M., Grippo, M. A., Heath, G. A., Macknick, J., Smith, K. P., Sullivan, R. G., Walston, L. J., & Wescott, K. L. (2016). *Understanding Emerging Impacts and Requirements Related to Utility-Scale Solar Development*. https://doi.org/10.2172/1329640

Herrmann, I., Bdolach, E., Montekyo, Y., Rachmilevitch, S., Townsend, P. A., & Karnieli, A. (2020). Assessment of maize yield and phenology by drone-mounted superspectral camera. *Precision Agriculture*, *21*(1), 51–76. https://doi.org/10.1007/S11119-019-09659-5/FIGURES/7

IEA. (2021). *World Energy Outlook 2021*. https://www.iea.org/reports/world-energy-outlook-2021

Iglhaut, J., Cabo, C., Puliti, S., Piermattei, L., O'Connor, J., & Rosette, J. (2019). Structure from
Motion Photogrammetry in Forestry: a Review. *Current Forestry Reports*, *5*(3), 155–168.
https://doi.org/10.1007/S40725-019-00094-3/FIGURES/4

Kim, D., Youn, J., & Kim, C. (2016a). Automatic detection of malfunctioning photovoltaic
modules using unmanned aerial vehicle thermal infrared images. *Journal of the Korean
Society of Surveying, Geodesy, Photogrammetry and Cartography*, *34*(6), 619–627.
https://doi.org/10.7848/ksgpc.2016.34.6.619

Kim, D., Youn, J., & Kim, C. (2016b). Automatic photovoltaic panel area extraction from UAV
thermal infrared images. *Journal of the Korean Society of Surveying, Geodesy,
Photogrammetry and Cartography*, *34*(6), 559–568.
https://doi.org/10.7848/ksgpc.2016.34.6.559

Kim, D., Youn, J., & Kim, C. (2017). Automatic fault recognition of photovoltaic modules based
on statistical analysis of UAV thermography. *International Archives of the
Photogrammetry, Remote Sensing and Spatial Information Sciences - ISPRS Archives*,
42(2W6), 179–182. https://doi.org/10.5194/isprs-archives-XLII-2-W6-179-2017

Kotivuori, E., Kukkonen, M., Mehtätalo, L., Maltamo, M., Korhonen, L., & Packalen, P. (2020).
Forest inventories for small areas using drone imagery without in-situ field measurements.
Remote Sensing of Environment, *237*, 111404. https://doi.org/10.1016/J.RSE.2019.111404

Leva, S., Aghaei, M., & Grimaccia, F. (2015). PV power plant inspection by UAS: Correlation
between altitude and detection of defects on PV modules. *2015 IEEE 15th International
Conference on Environment and Electrical Engineering, EEEIC 2015 - Conference
Proceedings*, 1921–1926. https://doi.org/10.1109/EEEIC.2015.7165466

Lu, K., Xu, R., Li, J., Lv, Y., Lin, H., & Liu, Y. (2022). A Vision-Based Detection and Spatial

Localization Scheme for Forest Fire Inspection from UAV. *Forests 2022, Vol. 13, Page 383*, *13*(3), 383. https://doi.org/10.3390/F13030383

Luo, X., Li, X., Yang, Q., Wu, F., Zhang, D., Yan, W., & Xi, Z. (2017). Optimal path planning for UAV based inspection system of large-scale photovoltaic farm. *Proceedings - 2017 Chinese Automation Congress, CAC 2017*, *2017-Janua*, 4495–4500. https://doi.org/10.1109/CAC.2017.8243572

Moreno-Garcia, I. M., Palacios-Garcia, E. J., Pallares-Lopez, V., Santiago, I., Gonzalez-Redondo, M. J., Varo-Martinez, M., & Real-Calvo, R. J. (2016). Real-Time Monitoring System for a Utility-Scale Photovoltaic Power Plant. *Sensors (Basel, Switzerland)*, *16*(6). https://doi.org/10.3390/S16060770

Mundaca, L., Sonnenschein, J., Steg, L., Höhne, N., & Ürge-Vorsatz, D. (2019). The global expansion of climate mitigation policy interventions, the Talanoa Dialogue and the role of behavioural insights. *Environmental Research Communications*, *1*(6), 61001. https://doi.org/10.1088/2515-7620/ab26d6

Nie, J., Luo, T., & Li, H. (2020). Automatic hotspots detection based on UAV infrared images for large-scale PV plant. *Electronics Letters*, *56*(19), 993–995. https://doi.org/10.1049/el.2020.1542

Ochiai, H., & Ikegami, H. (2016). PPLC-PV: A pulse power line communication for series-connected PV monitoring. *2016 IEEE International Conference on Smart Grid Communications, SmartGridComm 2016*, 338–344. https://doi.org/10.1109/SMARTGRIDCOMM.2016.7778784

Ong, S., Campbell, C., Denholm, P., Margolis, R., & Heath, G. (2013). *Land-Use Requirements for Solar Power Plants in the United States*. www.nrel.gov/publications.

Orduz, R., Solõrzano, J., Egido, M. Á., & Román, E. (2013). Analytical study and evaluation results of power optimizers for distributed power conditioning in photovoltaic arrays. *Progress in Photovoltaics: Research and Applications*, *21*(3), 359–373. https://doi.org/10.1002/PIP.1188

Pecci, A. (2020). Digital survey from drone in archaeology: potentiality, limits, territorial archaeological context and variables. *IOP Conference Series: Materials Science and Engineering*, *949*(1), 012075. https://doi.org/10.1088/1757-899X/949/1/012075

Quater, P. B., Grimaccia, F., Leva, S., Mussetta, M., & Aghaei, M. (2014). Light Unmanned Aerial Vehicles (UAVs) for cooperative inspection of PV plants. *IEEE Journal of Photovoltaics*, *4*(4), 1107–1113. https://doi.org/10.1109/JPHOTOV.2014.2323714

Santangeli, A., Chen, Y., Kluen, E., Chirumamilla, R., Tiainen, J., & Loehr, J. (2020). Integrating drone-borne thermal imaging with artificial intelligence to locate bird nests on agricultural land. *Scientific Reports 2020 10:1*, *10*(1), 1–8. https://doi.org/10.1038/s41598-020-67898-3

Shariati, M., Mesgari, T., Kasraee, M., & Jahangiri-rad, M. (2020). Spatiotemporal analysis and hotspots detection of COVID-19 using geographic information system (March and April, 2020). *Journal of Environmental Health Science and Engineering*, *18*(2), 1499–1507. https://doi.org/10.1007/S40201-020-00565-X/FIGURES/6

Sirat, E. F., Setiawan, B. D., & Ramdani, F. (2019). Comparative Analysis of K-Means and Isodata Algorithms for Clustering of Fire Point Data in Sumatra Region. *2018 4th International Symposium on Geoinformatics, ISyG 2018*. https://doi.org/10.1109/ISYG.2018.8611879

Smith, K. W. (2015). Drone Technology: Benefits, Risks, and Legal Considerations. *Seattle*

Journal of Environmental Law (SJEL), 5.

https://heinonline.org/HOL/Page?handle=hein.journals/sjel7&id=312&div=14&collection=journals

Spagnolo, G. S., Del Vecchio, P., Makary, G., Papalillo, D., & Martocchia, A. (2012). A review of IR thermography applied to PV systems. *2012 11th International Conference on Environment and Electrical Engineering, EEEIC 2012 - Conference Proceedings*, 879–884. https://doi.org/10.1109/EEEIC.2012.6221500

Tamminga, A., Hugenholtz, C., Eaton, B., & Lapointe, M. (2015). Hyperspatial Remote Sensing of Channel Reach Morphology and Hydraulic Fish Habitat Using an Unmanned Aerial Vehicle (UAV): A First Assessment in the Context of River Research and Management. *River Research and Applications*, *31*(3), 379–391. https://doi.org/10.1002/RRA.2743

Tauro, F., Petroselli, A., & Arcangeletti, E. (2016). Assessment of drone-based surface flow observations. *Hydrological Processes*, *30*(7), 1114–1130. https://doi.org/10.1002/HYP.10698

Tsanakas, J. A., Vannier, G., Plissonnier, A., Ha, D. L., & Barruel, F. (2015). Fault diagnosis and classification of large-scale photovoltaic plants through aerial orthophoto thermal mapping. *31st European Photovoltaic Solar Energy Conference and Exhibition*, *November*, 1783–1788.

U.S. Energy Information Administration. (2022). Annual Energy Outlook 2022. *EIA*. https://www.eia.gov/outlooks/aeo/pdf/AEO2022_Narrative.pdf

Varghese, A., Gubbi, J., Sharma, H., & Balamuralidhar, P. (2017). Power infrastructure monitoring and damage detection using drone captured images. *Proceedings of the International Joint Conference on Neural Networks*, *2017-May*, 1681–1687.

https://doi.org/10.1109/IJCNN.2017.7966053

Vergura, S., Marino, F., & Carpentieri, M. (2015). Processing infrared image of PV modules for defects classification. *2015 International Conference on Renewable Energy Research and Applications, ICRERA 2015*, 1337–1341. https://doi.org/10.1109/ICRERA.2015.7418626

Vetrivel, A., Gerke, M., Kerle, N., & Vosselman, G. (2015). Identification of damage in buildings based on gaps in 3D point clouds from very high resolution oblique airborne images. *ISPRS Journal of Photogrammetry and Remote Sensing*, *105*, 61–78. https://doi.org/10.1016/J.ISPRSJPRS.2015.03.016

Yang, Y., & Lee, X. (2019). Four-band thermal mosaicking: A new method to process infrared thermal imagery of urban landscapes from UAV flights. *Remote Sensing*, *11*(11). https://doi.org/10.3390/rs11111365

Zhang, C., Luo, L., Xu, W., & Ledwith, V. (2008). Use of local Moran's I and GIS to identify pollution hotspots of Pb in urban soils of Galway, Ireland. *Science of The Total Environment*, *398*(1–3), 212–221. https://doi.org/10.1016/J.SCITOTENV.2008.03.011